



ELSEVIER

Journal of Nuclear Materials 270 (1999) 96–114

Journal of
nuclear
materials

Section 2. Cladding and structural materials

Microchemistry and microstructure of proton-irradiated austenitic alloys: toward an understanding of irradiation effects in LWR core components

G.S. Was^{a,*}, T.R. Allen^a, J.T. Busby^a, J. Gan^a, D. Damcott^a, D. Carter^a,
M. Atzmon^a, E.A. Kenik^b

^a Department of Nuclear Engineering and Radiological Sciences, College of Engineering, University of Michigan, 1911 Cooley Building, 2355 Bonisteel Boulevard, Ann Arbor, MI 48109-2104, USA

^b Oak Ridge National Laboratory, Metals and Ceramics Division, Oak Ridge, TN, USA

Received 9 June 1998; accepted 12 October 1998

Abstract

Over 1200 measurements of grain boundary composition and microstructure have been made on 14 different austenitic Fe–Cr–Ni alloys following proton irradiation in the temperature range 200–600°C and in the dose range 0.1–3.0 dpa. From these data, a greater understanding of radiation induced segregation (RIS) and microstructure development has been gained. Grain boundary composition measurements revealed that Cr depletes at grain boundaries, Ni enriches and Fe can either enrich or deplete depending on alloy composition. Analysis of temperature and composition dependence of RIS revealed that the magnitude and direction of grain boundary segregation depends on alloy composition because the values of migration enthalpy of the alloy constituents are not the same, and diffusivities of the alloy constituents are composition-dependent. The dose dependence of segregation revealed ordering in Ni-base alloys and temperature dependence was used to show that RIS is consistent with a vacancy exchange mechanism. The dependence of segregation on composition is consistent with all known, relevant neutron data. RIS was found to be related to the development of the dislocation and void microstructures. Alloys in which the microstructure develops slower with dose also show slower changes in RIS. Similarly, it was shown that the dependence of swelling on composition is the same for neutron, ion and proton irradiation and all can be explained by the effect of RIS on defect diffusivity at the void nuclei. This paper illustrates the value of conducting carefully chosen irradiation experiments over several, well-controlled variables to elucidate the mechanisms underlying the microchemical and microstructural changes. © 1999 Elsevier Science B.V. All rights reserved.

1. Introduction

Irradiation effects in materials used in nuclear reactor applications has been a subject of ongoing study for the past 40 yr. Yet, despite the widespread use of austenitic alloys in light water reactor (LWR) cores, the (open literature) database on the effects of irradiation on the microstructure and microchemistry under LWR condi-

tions is amazingly sparse. In contrast, both the size of the database and the level of understanding of microstructure development under conditions relevant to fast reactors is considerably better. The difference between these applications is significant as fast reactors operate in the temperature range 450–600°C, and at doses over 100 dpa. Conversely, light water reactor core materials typically experience temperatures in the range 270–330°C and dose in the range 0–10 dpa. Because these databases are mutually exclusive, attempts to project microstructure and microchemistry development of the same alloy under LWR conditions using fast reactor irradiation conditions are unreliable.

* Corresponding author. Tel.: +1-313 763 4675; fax: +1-313 763 4540; e-mail: gsw@umich.edu

The impetus for understanding irradiation effects on microstructure and microchemistry in austenitic alloys under LWR irradiation conditions is the persistence of core component failures which are attributed, at least in part, to irradiation effects. An example is the phenomenon of irradiation assisted stress corrosion cracking (IASCC), in which material changes due to irradiation are known to be important [1]. Without an adequate database on irradiation effects under relevant conditions, there is little hope of successfully addressing this problem. Hence, in recent years, increased attention has been focused on acquiring a better understanding of the development of both the microstructure and the microchemistry of austenitic alloys under LWR conditions.

An impediment to this objective is the cost and time required for neutron irradiation, either in power or test/research reactors. Consequently, there has been increasing interest in the use of light ions to emulate the effects of neutron irradiation in a light water reactor core. An extensive program has been conducted over the last 10 yr which has sought to characterize proton irradiation effects, establish a correlation with neutron irradiation effects and utilize the growing database to improve our understanding about the physical processes underlying the development of the microchemistry and microstructure of austenitic alloys irradiated under LWR conditions. This paper presents a comprehensive compilation of the microstructure and microchemistry changes produced by proton irradiation of austenitic alloys under conditions relevant to LWR core components. Most of the data have appeared elsewhere in focused studies addressing one or more of the underlying physical processes controlling radiation-induced segregation or the formation of the dislocation and void microstructures under irradiation [1–34]. The purpose of this paper is to present the complete dataset on microstructure and microchemistry changes resulting from proton irradiation, to establish the dose, temperature and alloy dependence, to compare results with those from light water reactors (where available), and to highlight some of the key results that have improved our understanding of the mechanisms of radiation induced segregation and radiation microstructures.

2. Experiment

2.1. Alloys

Alloys used in this program were austenitic iron- and nickel-base alloys with varying impurity levels made by the General Electric Company. Table 1 gives the major element compositions and the heat designations. The as-received alloys were solution annealed at 1100°C for 1 h to homogenize the microstructure, and were then cold-rolled to 2 mm thickness. Samples for irradiation were

cut from the rolled material for both AES (2.5×2 mm) and TEM (4×2 mm) analysis. These samples were wet polished with silicon carbide paper and given a 0.5–1 h recrystallization anneal at 850°C to achieve a grain size of approximately 10 μm . After annealing the samples were again wet polished and electropolished in a 60% phosphoric + 40% sulfuric acid solution at -50°C to provide a smooth surface finish prior to irradiation. Samples for Auger analysis are notched on one side to a depth of 0.5 mm.

2.2. Proton irradiation

Sample irradiations were performed using a specially designed stage connected to the General Ionex Tandetron accelerator at the Michigan Ion Beam Laboratory for Surface Modification and Analysis at the University of Michigan [5]. Irradiations were conducted using 3.2 MeV protons at a dose rate of approximately 7×10^{-6} dpa/s (the experimental doses and dose rates are calculated using TRIM97 [35]), resulting in a nearly uniform damage rate through the first 35 μm of the proton range (40 μm). Irradiations were conducted in a vacuum of better than 3×10^{-8} torr.

Samples are fixed to the stage using cylindrical hold-down bars. Multiple samples can be irradiated simultaneously, providing duplicate samples for the same experimental conditions. The total sample width that can be irradiated is 16 mm. Thus, the irradiation stage design allows for flexibility in the number and type of samples loaded during a given irradiation.

The irradiation stage is electrically isolated from the beamline and four rectangular tantalum apertures are used to define the area of the sample bars that is irradiated with the proton beam. The proton beam (approximately 3 mm in diameter) is rastered across the stage so that about half the total beam current is deposited on the samples and half on the apertures. This rastering ensures that samples at any position on the stage receive the same dose. Additionally, the proton beam is centered by balancing the amount of current on each of the four apertures.

The irradiation stage is designed to control the sample temperature by controlling the stage temperature. The stage is heated using a resistive cartridge heater and cooled using room temperature air flowing through cooling lines that penetrate the back of the stage. The stage surface is made of copper to provide good heat conduction away from the samples. To provide effective thermal contact between the sample bars and the stage, a thin layer of tin (for irradiations at or above 400°C) or indium (for irradiations below 400°C) is placed between the samples and the stage surface. The metal is molten at the irradiation temperature, maximizing the thermal contact between samples and stage. Sample temperature was monitored using two techniques. Type J (iron/con-

Table 1

Summary of grain boundary composition measurements of Fe, Ni and Cr in several austenitic alloys irradiated with 3.2 MeV protons (uncertainty given as the standard deviation of the mean σ/\sqrt{N})

Alloy	Heat	Temp (°C)	Dose (dpa)	Meas. type	No. of Samples	No. of Meas.	Iron (at.%)	Chromium (at.%)	Nickel (at.%)	Refs.
Ni-18Cr	RAM	—	0	AES	1	12	—	17.1 ± 0.2	82.9 ± 0.2	[3]
	1201	—	0	STEM	1	15	—	18.8 ± 0.2	81.2 ± 0.2	[3]
		200	0.5	AES	2	28	—	14.6 ± 0.2	85.4 ± 0.2	[3]
		300	0.5	AES	2	33	—	11.5 ± 0.2	88.5 ± 0.2	[3]
		400	0.1	AES	2	33	—	13.4 ± 0.3	86.6 ± 0.3	[3]
		400	0.1	STEM	2	22	—	15.7 ± 0.2	84.3 ± 0.2	[3]
		400	0.3	AES	2	32	—	11.8 ± 0.2	88.2 ± 0.2	[3]
		400	0.3	STEM	2	34	—	14.3 ± 0.3	85.7 ± 0.3	[3]
		400	0.5	AES	5	62	—	10.1 ± 0.2	89.9 ± 0.2	[3]
		400	0.5	STEM	2	33	—	13.0 ± 0.3	87.0 ± 0.3	[3,24]
		400	1.0	AES	2	36	—	10.6 ± 0.3	89.4 ± 0.3	[3]
		400	1.0	STEM	1	15	—	13.6 ± 0.3	86.4 ± 0.3	[3]
		500	0.5	AES	2	23	—	12.9 ± 0.5	87.1 ± 0.5	[3]
	Ni-18Cr-9Fe	RAM	—	0	AES	2	12	9.4 ± 0.3	18.0 ± 0.4	72.6 ± 0.5
1202		—	0	STEM	1	17	9.2 ± 0.1	17.9 ± 0.2	72.8 ± 0.2	[3,16]
		200	0.5	AES	1	16	6.7 ± 0.5	15.7 ± 0.2	77.6 ± 0.5	[3]
		300	0.5	AES	1	14	5.4 ± 0.5	13.8 ± 0.3	80.8 ± 0.6	[3]
		400	0.1	AES	3	25	5.2 ± 0.2	13.9 ± 0.2	80.9 ± 0.2	[3]
		400	0.1	STEM	2	22	6.6 ± 0.1	16.0 ± 0.2	77.4 ± 0.3	[3,16]
		400	0.3	AES	2	23	4.9 ± 0.3	13.9 ± 0.4	81.1 ± 0.4	[3]
		400	0.3	STEM	2	34	5.8 ± 0.1	15.4 ± 0.2	78.7 ± 0.2	[3,16,24]
		400	0.5	AES	2	27	5.8 ± 0.3	13.5 ± 0.2	80.7 ± 0.5	[3]
		400	0.5	STEM	2	45	5.4 ± 0.1	14.4 ± 0.2	80.2 ± 0.3	[3,16]
		400	1.0	AES	2	27	5.5 ± 0.3	13.8 ± 0.3	80.7 ± 0.6	[3]
		400	1.0	STEM	1	20	5.8 ± 0.2	15.3 ± 0.2	78.7 ± 0.3	[3,16]
		500	0.5	AES	2	30	6.5 ± 0.3	15.7 ± 0.2	77.8 ± 0.5	[3]
Fe-20Cr-24Ni		RAM	—	0	STEM	1	20	55.4 ± 0.1	20.1 ± 0.1	23.3 ± 0.1
	1155	200	1.0	AES	1	11	53.5 ± 0.8	20.8 ± 0.6	25.8 ± 0.8	[3,6]
		300	0.5	AES	3	33	53.7 ± 0.6	19.3 ± 0.7	27.0 ± 0.4	[3,6]
		400	0.1	AES	2	35	55.2 ± 0.3	18.0 ± 0.2	26.9 ± 0.3	[3,6]
		400	0.5	AES	2	21	52.0 ± 1.0	13.6 ± 0.3	34.5 ± 1.0	[3,6]
		400	0.5	STEM	1	10	52.3 ± 0.5	14.0 ± 0.3	32.6 ± 0.7	[3,16]
		400	1.0	AES	3	38	51.9 ± 0.7	12.1 ± 0.4	36.0 ± 0.8	[3,6]
		400	1.0	STEM	2	50	50.6 ± 0.5	14.0 ± 0.2	35.1 ± 0.7	[3,16]
		400	3.0	AES	3	39	47.6 ± 0.9	14.1 ± 0.6	38.4 ± 1.1	[3,6]
		400	3.0	STEM	2	30	51.7 ± 0.3	14.5 ± 0.1	33.4 ± 0.4	[3,16]
		500	0.5	AES	3	36	48.4 ± 1.2	13.0 ± 0.9	38.6 ± 0.5	[3,6]
		600	0.5	AES	2	27	55.2 ± 0.4	17.9 ± 0.3	26.8 ± 0.5	[3]
	Fe-18Cr-8Ni (CP 304 SS)	—	0	STEM	2	18	68.2 ± 0.2	20.5 ± 0.2	8.0 ± 0.1	
360		0.3	STEM	1	8	67.9 ± 0.4	19.5 ± 0.2	9.4 ± 0.1		
360		1.0	STEM	3	50	68.3 ± 0.2	18.7 ± 0.1	9.2 ± 0.1		
Fe-16Cr-13Ni (CP 316 SS)	—	0	STEM	3	35	58.5 ± 0.3	19.8 ± 0.1	10.3 ± 0.1		
	360	1.0	STEM	4	32	57.9 ± 0.1	17.2 ± 0.1	13.9 ± 0.1		
Fe-20Cr-9Ni	RAM	—	0	AES	1	12	68.7 ± 0.3	23.2 ± 0.4	8.1 ± 0.1	[3]
	1327	—	0	STEM	1	23	68.7 ± 0.1	21.1 ± 0.1	9.1 ± 0.0	[3,16]
		335	1.0	STEM	1	25	70.0 ± 0.1	19.4 ± 0.1	9.6 ± 0.6	
		360	1.0	STEM	1	23	71.4 ± 0.1	16.3 ± 0.2	11.8 ± 0.3	
		400	0.1	AES	3	25	69.4 ± 0.2	21.4 ± 0.3	9.2 ± 0.2	[3]

Table 1 (Continued)

Alloy	Heat	Temp (°C)	Dose (dpa)	Meas. type	No. of Samples	No. of Meas.	Iron (at.%)	Chromium (at.%)	Nickel (at.%)	Refs.
		400	0.1	STEM	1	23	69.9 ± 0.1	19.9 ± 0.1	9.5 ± 0.1	[3,16]
		400	0.1	STEM ^a	1	5	71.3 ± 0.5	16.5 ± 0.5	12.2 ± 0.5	
		400	0.5	STEM	1	29	70.0 ± 0.2	18.9 ± 0.2	10.3 ± 0.2	[3]
		400	3.0	AES	2	24	66.4 ± 0.4	9.0 ± 0.4	24.6 ± 0.6	[3,16]
		400	3.0	STEM	1	16	70.3 ± 0.8	13.8 ± 0.3	15.5 ± 0.8	[3,16]
		400	3.0	STEM ^a	1	5	70.6 ± 0.4	10.8 ± 0.5	18.5 ± 0.3	
Fe-20Cr-9Ni (UHP)	BPV	400	1.0	AES	5	65	70.3 ± 0.2	17.0 ± 0.2	12.7 ± 0.2	[8,10]
	945	400	1.0	STEM	2	26	71.5 ± 0.1	17.1 ± 0.2	11.0 ± 0.2	[8,10]
							P (at.%)			
Fe-20Cr-9Ni-P (UHP+P)	BPV	—	0	AES	4	8	5.3 ± 0.4	21.7 ± 0.7	8.8 ± 0.5	[10]
	603	400	1.0	AES	7	34	8.7 ± 0.4	15.0 ± 0.4	13.8 ± 0.5	[8,10]
		400	1.0	STEM	1	12	1.8 ± 0.1	17.1 ± 0.4	12.4 ± 0.3	[8,10]
							S (at.%)			
Fe-20Cr-9Ni-S (UHP+S)	BPV	400	1.0	AES	5	42	ND ^b	15.0 ± 0.5	15.5 ± 0.5	[8,10]
	946	400	1.0	STEM	1	18	ND	16.1 ± 0.2	12.0 ± 0.2	[8,10]
							Si (at.%)			
Fe-20Cr-9Ni-Si (UHP+Si)	BPV	400	0.1	STEM	1	33	1.35 ± 0.1	18.4 ± 0.1	9.5 ± 0.1	
	604	400	1.0	STEM	1	27	2.8 ± 0.2	14.8 ± 0.2	12.8 ± 0.3	[8,10]
Fe-16Cr-24Ni	RAM	400	1.0	AES	3	27	50.5 ± 0.7	10.7 ± 0.4	38.9 ± 1.0	[6]
	1177									
Fe-24Cr-19Ni	RAM	400	1.0	AES	2	23	57.1 ± 0.4	17.2 ± 0.7	25.7 ± 0.4	[3,6]
	1152									
Fe-24Cr-24Ni	RAM	400	1.0	AES	3	36	49.8 ± 0.5	14.7 ± 0.5	35.4 ± 0.7	[3,6]
	1151									
							P (at.%)			
Ni-18Cr-P	RAM	—	0	AES	1	10	9.00 ± 0.4	14.0 ± 0.2	76.9 ± 0.3	[2]
	1203	400	0.5	AES	2	24	12.2 ± 0.3	8.7 ± 0.1	79.2 ± 0.4	[2]

Note: Sum of Fe + Cr + Ni: does not necessarily equal 100%.

^a STEM measurements taken using Philips CM200/FEG.

^b ND: Not detected.

stantine) thermocouples were spot welded directly to AES sample surfaces to provide one temperature measurement. Typically, three to five thermocouples are attached to the samples during any one irradiation. A separate thermocouple monitors the temperature at the back of the stage. In addition to the thermocouples, a calibrated infrared pyrometer monitors the surface of the samples during irradiation. The pyrometer can also be controlled remotely to scan the surface of the specimens to insure temperature uniformity. The pyrometer is calibrated prior to irradiation by heating the samples to the irradiation temperature and adjusting the pyrometer's emissivity setting so that the pyrometer reading matched that of the thermocouples. During irradiation, the sample temperature is controlled to

±10°C on either side of the target temperature by controlling the amount of heating and/or cooling to the stage. By providing a large fraction of the total heat input to the samples from the stage, temperature fluctuations due to beam current fluctuations are minimized.

Experimental parameters are tracked continuously during the irradiation using a PC-based monitoring system. The monitoring software tracks and records the stage current, aperture currents, pyrometer temperature and up to five thermocouple temperatures. This system allows the operator to continuously monitor experimental parameters while also providing a comprehensive history of each irradiation. Alarms are also available to alert the operator when experimental parameters have moved outside acceptable limits.

Following irradiation, samples have significant β activity that decays exponentially with time. This activity is the result of isotopes created in (p,n) reactions between the proton beam and the constituents of the target. This residual activity is measured and used to insure that the samples are irradiated uniformly across the stage. Samples from the same irradiation which have an activity that varies by greater than 10% are excluded from analysis [20].

2.3. Grain boundary composition measurements

Grain boundary composition in irradiated samples was measured using two different methods, Auger electron spectroscopy (AES) and scanning transmission electron microscopy with energy dispersive X-ray spectroscopy (STEM/EDS). Both AES and STEM/EDS are sensitive enough to measure the narrow (5–10 nm wide) RIS profiles, but because both average over a rapidly changing portion of the segregation profile, they underestimate the difference between grain boundary and bulk concentrations. AES is suitable for measuring the grain boundary composition because the escape depth for Auger electrons is on the order 7–10 monolayers. AES is not used to measure grain boundary profiles because of the difficulty in sputtering intergranular facets that lie at random angles to the sputter gun and the cylindrical mirror analyzer. Rather, grain boundary composition profiles were measured in STEM/EDS by using a narrow (about 2 nm) electron beam to probe a region near the grain boundary. Because the finite width of the STEM electron beam is greater than the Auger electron escape depth, STEM/EDS is not quite as sensitive to grain boundary chemistry as AES. STEM/EDS is significantly more time consuming than AES, but it provides an important complementary measurement to the AES data.

2.3.1. Auger electron spectroscopy

AES samples were analyzed in a PHI 660 Scanning Auger Microprobe located at Ford Research and Development Center, Dearborn, MI. To measure grain boundary chemistry using AES, the sample must fracture intergranularly. To promote intergranular fracture, the samples are cathodically charged with hydrogen at 20–30°C at a current density of 0.5 A/cm² in a solution of 0.1 N sulfuric acid with 0.1 g of sodium arsenite added as a recombination poison. The samples are charged with hydrogen for a minimum of 72 h and stored in liquid nitrogen until analyzed. The PHI 660 has an in situ fracture stage integral to the SAM. The fracture stage was cooled with methanol and dry ice for 45 min to drop the temperature of the fracture stage to around 0°C. Samples are loaded into the fracture stage and cooled for 30 min prior to fracture. To expose fresh grain boundary facets, the samples are fractured in a vacuum of less than 1×10^{-8} torr. The sample bar was notched to ensure that

the irradiated face opens upon straining the sample. The samples are slowly strained (over a 10 min period) which allows the retained hydrogen to diffuse to the crack tip and aids in promoting intergranular fracture. In the majority of cases, the samples did not completely fracture in half, but cracks opened wide enough to image irradiated grain boundaries.

The grain boundaries chosen to be analyzed were located away from the surface to minimize the effect of surface segregation and oxidation. Grain facets selected for analysis were required to be at least 5 μ m in diameter to allow for some sample drift while maintaining the microprobe on the grain facet. Typically, grain boundaries chosen for analysis were selected from an area of the sample with two-to-four exposed boundaries. This decreased the time to acquire spectra by allowing for the analysis of multiple boundaries in the same scan.

All spectra were collected using a beam energy of 10 keV. To increase the peak-to-background signal ratio for analysis of the other alloys, the condenser and focusing elements were adjusted to increase the beam current to approximately 100 nA. To maintain proper positioning during these adjustments, contrast features for each acquisition were outlined with a marker on the display screen and the image position was corrected as the focus and condenser settings were changed.

To identify the peaks of interest for analysis, a survey is performed which identifies all significant peaks between 0 and 2100 eV. From the survey, peaks are chosen from which to perform multiplex analysis. In multiplex mode, data is only recorded about the energies of the peaks of interest. For all Fe–Cr–Ni alloys, Cr and Ni are analyzed using the 529 eV Cr peak and the 848 eV Ni peak. For the Fe-base alloy, the 703 eV Fe peak is used. However, because of overlap of the 703 eV Fe and the 690 eV Ni peaks in Ni–18Cr–9Fe, the 651 eV Fe peak was used to measure Fe concentrations in the Ni-base alloys [36].

Samples were analyzed in the multiplex mode of the SAM, scanning for Fe, Cr, Ni, P, C, and O as appropriate for the sample being analyzed. A complete listing of all the parameters used to define each multiplex data collection is provided in Ref. [36]. C and O were analyzed to monitor the status of contamination of the exposed grain boundary facets. Because of overlap between the 529 eV Cr peak and the 513 eV O peak, data collection for each sample was terminated if the calculated O concentrations reached 15–20 at.%, limiting data collection to between eight and twenty grain boundaries per sample for an analysis period of about 2 h. A study by Damcott [6] indicated that the calculated Cr is not significantly affected if the measured O concentration is less than 25 at.%.

Once an AES spectrum has been gathered, the grain boundary concentration is calculated from the intensities using the following relationship [37]:

$$C_i = \frac{I_i/\lambda_i}{\sum I/\lambda}, \quad (1)$$

where I is the intensity of the signal for element i (as determined by the peak-to-peak height of the differentiated AES spectra) and λ is the relative sensitivity factor. Intensity profiles are not directly used to calculate concentrations. Because of the large background signal of backscattered and secondary electrons present at the detector in a SAM, the intensity peaks of the Auger electrons can be difficult to discern. Therefore, the intensity profile is differentiated with respect to energy to highlight the Auger peaks, and the peak-to-peak height of the differentiated spectrum is used as a measure of the intensity of each peak. The peak-to-peak height of the differentiated spectrum is assumed to be proportional to the area under the intensity profile (which is exact if the intensity profile is Gaussian in shape). If the AES peaks change shape from boundary to boundary, using the differentiated peak-to-peak height may generate slight errors when calculating concentrations. For this work, the sensitivity factors are calculated in the following manner. From Eq. (1)

$$\frac{I_i}{C_i \lambda_i} = \sum \frac{I}{\lambda} = \text{constant}. \quad (2)$$

For a given grain boundary measurement, the sum (over all elements in the alloy) of the intensity divided by the sensitivity factor is fixed. Therefore, for an Fe–Cr–Ni alloy

$$\frac{I_{\text{Cr}}}{C_{\text{Cr}} \lambda_{\text{Cr}}} = \frac{I_{\text{Ni}}}{C_{\text{Ni}} \lambda_{\text{Ni}}} = \frac{I_{\text{Fe}}}{C_{\text{Fe}} \lambda_{\text{Fe}}}. \quad (3)$$

The intensities I_{Cr} , I_{Ni} , and I_{Fe} are measured from an area of the sample that has fractured in a ductile manner. Assuming the concentrations C_{Cr} , C_{Ni} , and C_{Fe} are known from the bulk concentration measurements taken using electron microprobe analysis, the relative sensitivity factors can be calculated as follows:

$$\frac{\lambda_{\text{Cr}}}{\lambda_{\text{Ni}}} = \frac{I_{\text{Cr}} C_{\text{Ni}}}{I_{\text{Ni}} C_{\text{Cr}}} \quad \text{and} \quad \frac{\lambda_{\text{Fe}}}{\lambda_{\text{Ni}}} = \frac{I_{\text{Fe}} C_{\text{Ni}}}{I_{\text{Ni}} C_{\text{Fe}}}. \quad (4)$$

2.3.2. Energy dispersive spectroscopy in scanning transmission electron microscopy

The second method used to measure grain boundary concentrations is STEM/EDS. To prepare a sample for STEM/EDS analysis, the irradiated 4 mm wide TEM sample bar was back thinned (ground on the non-irradiated face) using 120 grit SiC grinding paper to a thickness of approximately 250 μm . Three millimeter discs were then cut using a slurry drill core cutter to minimize sample deformation. The 3 mm discs were mechanically back thinned to approximately 120 μm using 1200 and 2400 grit SiC grinding paper. Samples were jet thinned using solutions of perchloric acid and

methanol at approximately -55°C in a South Bay single jet electropolishing instrument.

STEM/EDS was performed at Oak Ridge National Laboratory on a Phillips EM400T/FEG equipped with an EDAX 9100/70 EDS system. An accelerating voltage of 100 kV was used. A double-tilt, liquid-nitrogen-cooled specimen holder was used to minimize contamination of the sample in the focused beam [38]. STEM/EDS measurements were performed at the grain boundary and at increments of 2.5 nm away from the boundary to provide composition profiles. The incident probe thickness was 2 nm (full width, tenth maximum). The sample was tilted toward the X-ray detector and each grain boundary analyzed was aligned such that the boundary was ‘edge-on’ (parallel to the electron beam). This placement ensured that the measured X-ray intensity had equal contributions from both sides of the boundary. The grain boundary was located by placing the electron probe in a position that generated equal portions of the diffraction patterns from each side of the boundary. Grain boundary profiles were performed by moving the probe a fixed distance from the boundary and measuring the X-ray intensity. All profiles were performed at a magnification of 2 000 000 \times . Because of sample drift, each acquisition was typically interrupted every 10 s to reposition the electron probe. Data acquisition lasted for 100 s of detector live time with counting rates of 1000–2000 counts/s for the X-rays from the entire sample.

Once a STEM/EDS spectrum (intensity of the K_α peak for each element versus energy) had been gathered, the concentration was calculated from the relative intensities of each element. For the alloys of this study, X-ray intensities were collected for the K_α peaks of Fe (7.114 keV), Cr (5.989 keV), and Ni (8.333 keV). To ensure the measured X-ray intensities were representative of only the sample and not the background of the microscope, a ‘hole-count’ spectrum was subtracted from the measured intensities prior to calculating the concentrations. A hole-count was performed by placing the electron probe in the sample perforation such that the probe travels through without interacting with the sample. X-rays were counted for 100 s, as in acquiring a spectrum from a sample. The ratio of the concentration of atom A to atom B was proportional to the ratio of the measured intensities, with the proportionality constant known as the k -factor:

$$\frac{C_A}{C_B} = k_{\text{AB}} \frac{I_A}{I_B}. \quad (5)$$

Similarly, the ratio of the concentration of atom B to atom C was proportional to the ratio of the measured intensities

$$\frac{C_B}{C_C} = k_{\text{BC}} \frac{I_B}{I_C}. \quad (6)$$

Assuming that

$$C_A + C_B + C_C = 1 \quad (7)$$

(that no other elements exist), the concentrations were calculated by simultaneously solving Eqs. (5)–(7). To calculate the k -factors, concentrations in the bulk of the material, away from the grain boundary segregation, were measured. The k -factors were chosen such that this bulk measurement corresponds to the bulk as measured by electron microprobe:

$$k_{AB} = \frac{C_A^{\text{microprobe}}}{C_B^{\text{microprobe}}} \frac{I_B^{\text{STEM/EDS}}}{I_A^{\text{STEM/EDS}}} \quad (8)$$

2.4. Microstructure

A JEOL2000FX transmission electron microscope was used for all microstructure characterization. TEM samples were prepared as described in the previous section. Quantitative analysis for dislocation loops was conducted using photos taken in bright field imaging mode with the two beam condition at $\mathbf{g} = [2\ 0\ 0]$ near the $[1\ 1\ 0]$ zone axis at a magnification of 100–200 kX. Weak beam dark field imaging was used to estimate the percentage of faulted loops. Voids were examined by tilting the sample away from the strong diffraction condition and varying the focus to optimize the image. Foil thickness was determined by using the contamination spot formed in spot mode on the STEM unit [39] or by using convergent beam electron diffraction (CBED) with the modified IMAGE computer program [40]. TEM photos were scanned into a TIF-format image file at 300 dpi resolution and analyzed using the software program PhotoShop®. The size and density of dislocation loops and voids were determined from these images.

A typical loop image had a nearly oval shape and the size was measured along its elongated direction. A typical void image had a cuboidal shape and the size was measured from edge to edge. The void number density was determined by counting the number of voids on an image with known thickness and tilt angle (and therefore, a known volume). The total dislocation loop density was determined in a two-step procedure. First, the percentage of faulted loops was determined from weak-beam dark-field imaging by ratioing the number of loops showing fringes (faulted loops) to the total number of loops, yielding the faulted loop fraction, F . At the $\mathbf{g} = [2\ 0\ 0]$ two-beam condition, all faulted loops and 2/3 of the perfect loops were visible [41]. Denoting this quantity as M , the total number of loops (faulted + perfect), N , is then $N = M/(F+2) (1-F)/3$. The total dislocation loop density ρ_t is N/V , and the faulted loop density, ρ_f is $\rho_t F$.

3. Results and discussion

3.1. Radiation induced segregation

Over 1200 grain boundary composition measurements have been made on 14 different austenitic Fe–Cr–Ni alloys, irradiated at temperatures ranging from 200°C to 600°C and to doses between 0.1 and 3.0 dpa. Table 1 lists the average grain boundary compositions, along with the number of boundaries and samples analyzed for each irradiation condition. The grain boundary composition measurements in Table 1 are as-measured, with no attempt to deconvolute the measurements for beam effects.

The trends in the segregation measurements for a specific alloy as a function of dose and temperature are similar for both the AES and STEM/EDS measurements. In each alloy, Cr depletes and Ni enriches at the grain boundary during irradiation. The difference between the STEM/EDS and AES grain boundary measurements is typically 2–3 at.% for Cr and 1–5 at.% for Ni, which is due to the difference in spatial resolution of the techniques, and is consistent with grain boundary concentrations measured in irradiated austenitic stainless steels using AES and STEM/EDS [8]. The consistency between the two independent measurements provides confidence that the measured trends are correct. In the following sections, the emphasis will be on a comparison between model calculations and AES measurements, but since the same trends are seen in the STEM/EDS measurements, the conclusions will hold for either type of measurement.

The results of grain boundary segregation under irradiation are shown in Figs. 1–10. Figs. 1–8 give the dose and temperature dependence of grain boundary composition for 4 different alloys. Fig. 9 presents the grain boundary composition changes as a function of

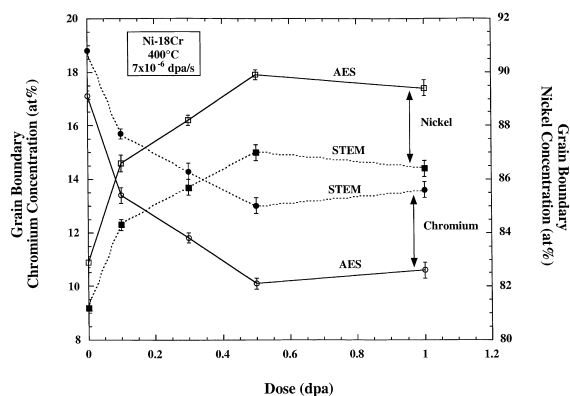


Fig. 1. Average grain boundary concentrations for Ni–18Cr irradiated at 400°C to various doses. Uncertainty bars are the standard deviation of the mean.

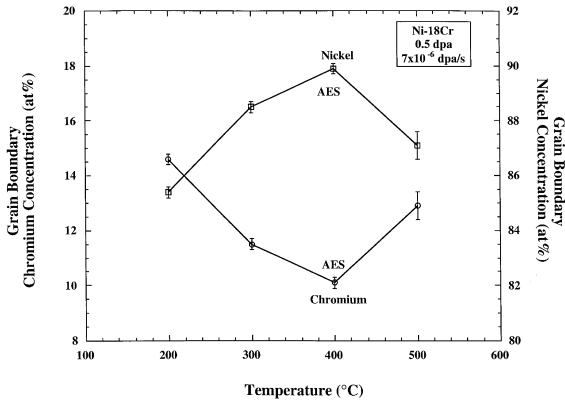


Fig. 2. Average grain boundary Cr concentration for Ni-18Cr irradiated to 0.5 dpa at various temperatures. Uncertainty bars are the standard deviation of the mean.

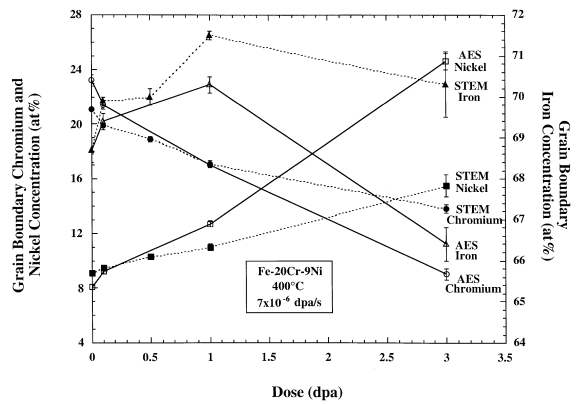


Fig. 5. Average grain boundary concentrations for Fe-20Cr-9Ni irradiated at 400°C to various doses. Uncertainty bars are the standard deviation of the mean.

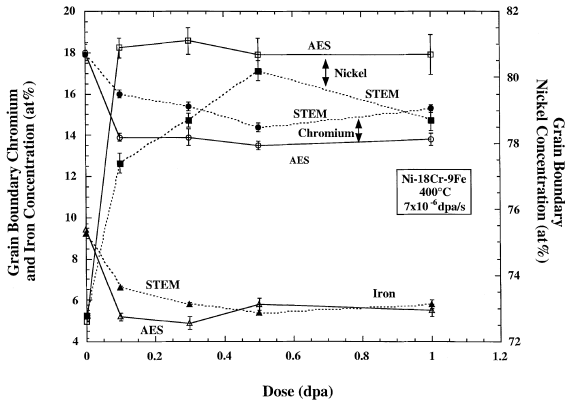


Fig. 3. Average grain boundary concentration for Ni-18Cr-9Fe irradiated at 400°C to various doses. Uncertainty bars are the standard deviation of the mean.

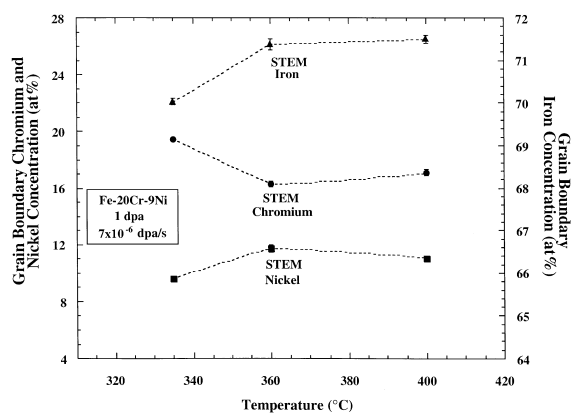


Fig. 6. Average grain boundary concentrations for Fe-20Cr-9Ni irradiated to 1 dpa at various temperatures. Uncertainty bars are the standard deviation of the mean.

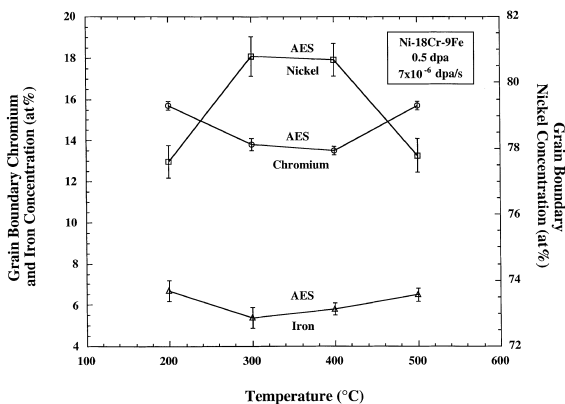


Fig. 4. Average grain boundary concentration for Ni-18Cr-9Fe irradiated to 0.5 dpa at various temperatures. Uncertainty bars are the standard deviation of the mean.

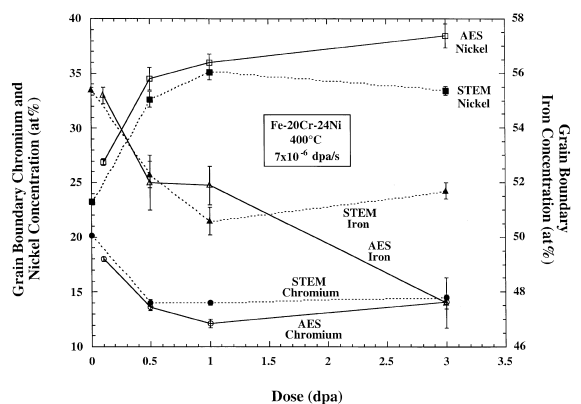


Fig. 7. Average grain boundary concentrations for Fe-20Cr-24Ni irradiated at 400°C to various doses. Uncertainty bars are the standard deviation of the mean.

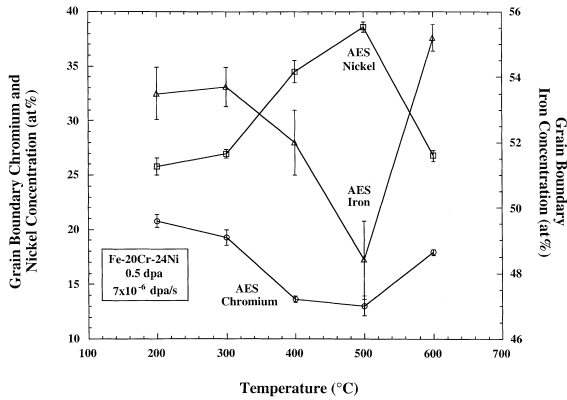


Fig. 8. Average grain boundary Cr concentration for Fe–20Cr–24Ni irradiated to 0.5 dpa at various temperatures. Uncertainty bars are the standard deviation of the mean.

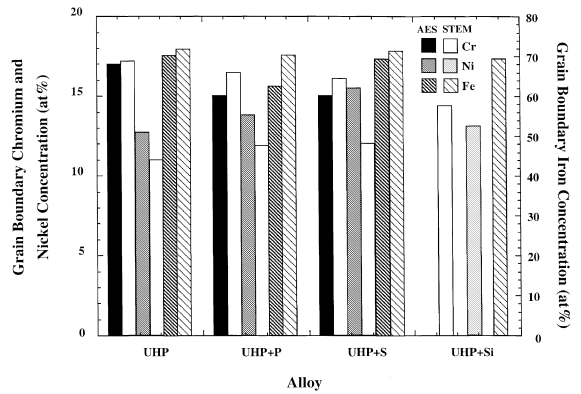


Fig. 10. Average grain boundary concentrations for UHP alloys irradiated at 400°C to 1.0 dpa. Uncertainty bars are the standard deviation of the mean.

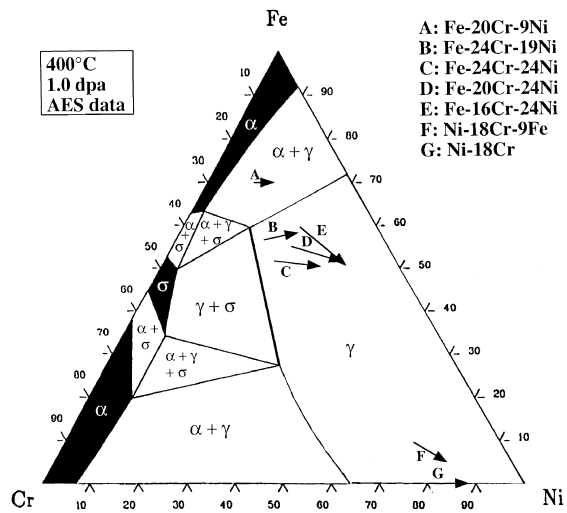


Fig. 9. Change in grain boundary concentration for seven alloys irradiated to 1.0 dpa at 400°C, superimposed on an Fe–Cr–Ni equilibrium phase diagram at 400°C.

alloy composition for 400°C, 1.0 dpa irradiations. Fig. 10 shows the grain boundary composition as a function of impurity element in high purity 304 heats.

Consistently, grain boundary Cr depletes and Ni enriches with increasing dose, and the behavior of Fe depends on the alloy, Figs. 1, 3, 5 and 7. Generally, when measurements are made by both AES and STEM, AES revealed greater segregation, due primarily to the better depth resolution of this technique as compared to the spatial resolution of current STEM units [8]. Figs. 2, 4, 6 and 8 show the characteristic bell-shaped dependence of segregation on temperature. Here again, grain boundary Cr went through a minimum and Ni went through a maximum and the behavior of Fe depended on the specific alloy.

As shown in Figs. 1–8 as well as in Fig. 9, there is a strong composition dependence of segregation. This is reflected in several features in these graphs including the degree of segregation at a given dose and temperature, the rate of segregation with dose, the shape of the temperature curve and the behavior of Fe among various alloys. Fig. 10 shows that the level of impurities affects the amount of segregation.

The analysis of grain boundary composition changes under irradiation has provided a significant and better understanding of the RIS mechanism in austenitic Fe–Cr–Ni alloys. This analysis was conducted by comparing grain boundary composition measurements to model predictions using the Perks model for grain boundary composition [42]. Segregation kinetics in this model are described using elemental diffusivities of the form

$$d_v^{Cr} = d_0^{Cr} \exp\left(\frac{-E_{tm}^{Cr}}{kT}\right). \tag{9}$$

The diffusivities are characterized by a pre-exponential factor, d_0^{Cr} and a migration energy, E_{tm}^{Cr} . These diffusivities are related to the self-diffusion coefficients by the relationship

$$D_{tsd}^{Cr} = C_v d_v^{Cr}. \tag{10}$$

Unless stated otherwise, the calculations were performed assuming that segregation was driven by preferential interaction of solute atoms with the vacancy flux. The diffusivities of atoms as interstitials are assumed equal. A detailed list of the input parameters used is given in Ref. [3].

The temperature dependence of segregation was used to determine information about the migration energies, the composition dependence of segregation was used to determine information about the pre-exponential factors, and dose dependence of segregation was used to determine information about ordering and the mecha-

nism of segregation. In particular, the following sections will show that (1) the migration energies of Cr, Ni, and Fe via vacancy exchange are not equal; the migration energy of Cr is greater than that of Fe which is greater than that of Ni, (2) segregation is composition dependent, (3) short range ordering forces are significant in determining the amount of segregation in Ni-rich alloys, and (4) the primary driving mechanism of RIS is the preferential interaction of solute atoms with the vacancy flux for both proton and neutron irradiated alloys. The following sections summarize the main accomplishments of this work. A complete analysis of each of the physical processes described below is provided in Refs. [3,4].

3.1.1. Migration energies of the alloy constituents are different

The temperature dependence of RIS in Fe–20Cr–24Ni and Ni–18Cr–9Fe was used to show that the migration energies of the alloy constituents are not the same [4]. Fig. 11 shows Cr and Ni grain boundary concentrations in Fe–20Cr–24Ni as a function of irradiation temperature for a dose of 0.5 dpa. Two cases are shown, one in which the vacancy migration energies of the alloy constituents are the same magnitude and one in which they differ. In both cases, the pre-exponential term in the expression for diffusivity in Eq. (9) was fixed, so as to isolate the effect of the migration energy on segregation. The standard treatment of migration energies in modeling of RIS in austenitic alloys [42] is to assign a single value to the migration energies of all the alloy

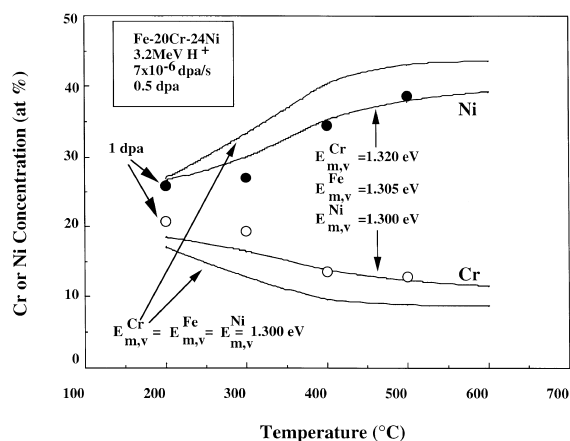


Fig. 11. Comparison of model calculations and AES measurements plotted with respect to temperature for an Fe–20Cr–24Ni alloy irradiated with protons at 7×10^{-6} dpa/s, 0.5 dpa, for a series of temperatures (200°C measurements from samples irradiated to 1 dpa). Reference calculation assumes all vacancy migration energies are equal to 1.3 eV. Model predictions are more accurate with Cr-vacancy migration energy of 1.32 eV, Fe-vacancy migration energy of 1.305 eV, and Ni-vacancy migration energy of 1.30 eV.

constituents and to ignore any effect of alloy composition on that value. Note that both the magnitude and shape of the temperature dependence of segregation are more accurately captured in the latter case than in the former. In fact, RIS is extremely sensitive to the value of the migration energy and small changes in migration energies can result in large changes in grain boundary composition. A detailed analysis of the sensitivity of the predicted grain boundary compositions with respect to the model input parameters was performed [26]. No other input parameter, varied within reasonable limits, could correct the model overpredictions. This case demonstrates that *migration energies of Fe, Cr and Ni in austenitic Fe–Cr–Ni alloys differ in magnitude, and this difference must be accounted for to properly predict RIS in this system.*

3.1.2. Diffusivities are dependent on alloy composition

The composition dependence of segregation was used to show that the diffusivities (specifically the pre-exponential factors) that describe the segregation are composition-dependent. Since segregation is determined by the relative diffusivities of Fe, Cr, and Ni, the composition dependence of diffusivity determines the composition dependence of segregation. Fig. 12 demonstrates how the composition dependence of diffusivities translates into composition dependence of segregation in Fe–Cr–Ni alloys. Grain boundary Ni compositions from five Fe–Cr–Ni alloys irradiated at 400°C to 1 dpa are compared to model calculations. Two sets of model calculations are performed. In one set, alloy-specific pre-exponential factors are determined by interpolation (Fe–

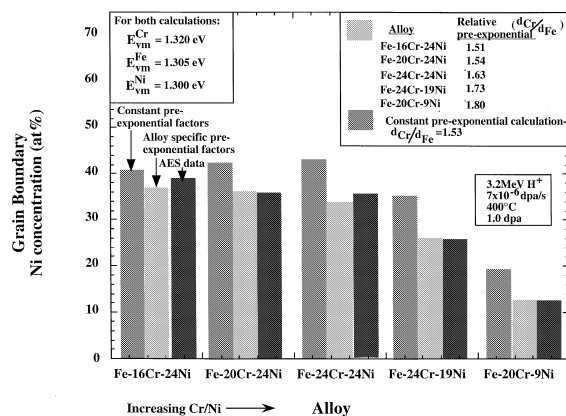


Fig. 12. Grain boundary Ni as a function of alloy composition. Grain boundary composition measured using AES is compared to model calculations assuming fixed pre-exponential factors with calculations assuming composition dependent pre-exponential factors. For both calculations, vacancy migration energies of 1.32 eV for Cr, 1.305 eV for Fe, and 1.30 eV for Ni are used. To accurately describe the segregation, alloy specific diffusivities are necessary.

16Cr–24Cr, Fe–20Cr–24Ni, Fe–24Cr–24Ni, and Fe–24Cr–19Ni) and extrapolation (Fe–20Cr–9Ni) of self-diffusion coefficients that were measured at high temperatures [43]. The second set of model calculations serves as a reference and assumes that the pre-exponential factors for Fe, Cr, and Ni do not change with alloy composition. For this set, constant diffusivity ratios of

$$\frac{d_v^{\text{Cr}}}{d_v^{\text{Ni}}} = 2.55, \quad \frac{d_v^{\text{Fe}}}{d_v^{\text{Ni}}} = 1.67, \quad \frac{d_v^{\text{Cr}}}{d_v^{\text{Fe}}} = 1.53$$

(corresponding to Fe–15Cr–20Ni) are used for all alloys. Both sets of calculations use migration energies of $E_{\text{vm}}^{\text{Cr}} = 1.32$, $E_{\text{vm}}^{\text{Fe}} = 1.305$, and $E_{\text{vm}}^{\text{Ni}} = 1.30$, as established in the previous section. As shown in the figure, both the magnitudes and trend of the measured grain boundary segregation agree much more closely with the composition-dependent diffusivities. Although changing other model parameters could possibly provide similar agreement, the diffusivities used in the alloy specific calculations were interpolated directly from measurements. The constant diffusivity calculation predicts an increase in the grain boundary Ni concentration with alloy Cr content, while experiment confirms the opposite trend, in agreement with calculations using composition-dependent diffusivities. The need for composition dependent pre-exponential factors is also evident from a detailed analysis of the relative segregation rates of Cr and Ni. This analysis is provided in Ref. [3]. *The diffusivities of Fe, Cr and Ni in austenitic Fe–Cr–Ni alloys depend on the bulk alloy compositions and these differences must be accounted for to properly predict RIS in these alloys.*

3.1.3. Dose dependence reveals ordering in Ni-base alloys and unique behavior of Fe in Fe–20Cr–9Ni

The dose dependence of segregation provides an indication that ordering may be influencing RIS, especially in Ni-base alloys. Under irradiation, the grain boundary composition becomes enriched in nickel and depleted in chromium. Fig. 13 shows the Cr:Ni exchange ratio at the grain boundary as a function of dose for Fe–20Cr–24Ni and Ni–18Cr–9Fe irradiated with protons at 400°C. The Cr:Ni exchange ratio is the number of Ni atoms arriving at the boundary for each Cr atom leaving (e.g., Cr:Ni ~ 0.5 means that on average, each Cr atom leaving is replaced by only 0.5 Ni atoms, requiring 0.5 Fe atoms as well). The exchange ratio was calculated by fitting a third order polynomial to a plot of grain boundary Ni versus grain boundary Cr. The slope of this plot is the exchange ratio. The 0 dpa exchange ratio was calculated by extrapolating the slope to 0 dpa. For Fe–20Cr–24Ni, model calculations indicate that at low dose, Cr leaves the boundary at a high rate, but this rate decreases with dose. At higher doses, when Cr is sufficiently depleted at the grain boundary, Fe becomes the

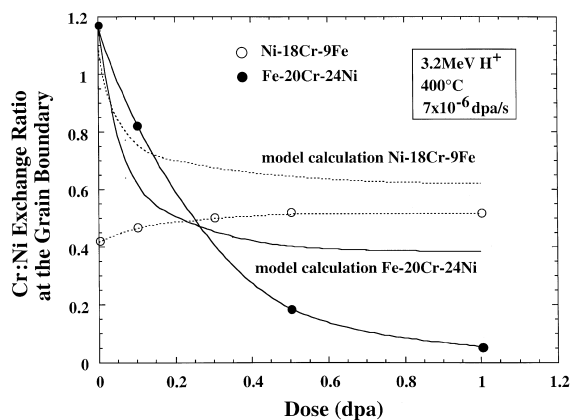


Fig. 13. Cr:Ni exchange ratio for Fe–20Cr–24Ni and Ni–18Cr–9Fe and comparison with calculations using the Perks model.

dominant element exchanging with Ni. Both measurement and model prediction agree on the dose (0.2 dpa) at which the Cr:Ni exchange ratio reaches the value of 0.5. The measurements in Fe–20Cr–24Ni are reasonably consistent with the model calculations, though the model does predict greater Cr depletion than is actually measured.

Conversely, segregation measurements in Ni–18Cr–9Fe disagree completely with model predictions. For Ni–18Cr–9Fe, which has a larger bulk Cr:Fe ratio (2:1) than does Fe–20Cr–24Ni (1:3), Cr:Ni replacements are always expected to be dominant. However, the Cr:Ni replacement ratio calculated from model predictions never reaches 0.5 and behaves opposite that of the measurement with increasing dose. The RIS data indicate that early in the irradiation of this alloy, Cr depletion is not as great as expected from calculation, but there is significant Fe depletion. In terms of exchange ratios, this means that the Cr:Ni exchange ratio is lower than expected and so the Fe:Ni ratio must be greater than expected, as shown in Fig. 13. This means that Fe diffuses at about the same rate as Cr in the Ni–18Cr–9Fe alloy, contrary to high temperature diffusion measurements [44] which show Cr to be the faster diffuser.

A possible explanation for the anomalous segregation behavior in Ni–18Cr–9Fe is short range ordering forces. Many measurements have shown ordering to occur in Fe–Cr–Ni alloys [45–48], with the strongest ordering occurring around the Ni–18Cr–9Fe composition. This tendency to form Ni–Cr pairs would slow down Cr segregation relative to that for Fe, causing the observed effect. Yet, the tendency to order would not be observed in high temperature diffusion measurements because the small ordering enthalpies would not be significant at high temperature. *These results show that short range ordering occurs in the nickel-rich end of the Fe–Cr–Ni ternary, and must be properly accounted for to accurately describe RIS.*

Of all the alloys studied, segregation of Fe in Fe–20Cr–9Ni is unique. The Fe–20Cr–9Ni alloy has a major element composition similar to 304 stainless steel. Because Fe initially enriches in this alloy at low dose, a larger Cr depletion occurs at high dose (as shown in Table 1). The large Cr depletion may make 304 stainless steel more susceptible to environmental cracking. From 0 to 1.0 dpa, Fe diffuses slower than the alloy average and therefore enriches at the grain boundary. Above 1.0 dpa, the change in composition near the boundary results in a drop of the local average below that of Fe. Fig. 14 plots Fe segregation as a function of dose for Fe–20Cr–9Ni irradiated at 400°C, along with model calculations using the Perks model. The Perks model predicts an increase in the grain boundary Fe concentration at low dose followed by a depletion at higher dose. The dose dependence predicted by the Perks model does not exactly follow the dose dependence of the data (the model predicts a maximum Fe concentration at a lower dose), but the predicted enrichment followed by depletion with increasing dose is confirmed by measurement. *Because the diffusivity of Fe is intermediate to Cr and Ni, enrichment/depletion of Fe is governed by the relative concentrations of these three alloy constituents.*

3.1.4. The segregation mechanism is by preferential exchange with vacancies

Segregation measurements were analyzed to determine the primary RIS mechanism in Fe–Cr–Ni alloys by comparing them to model predictions that assumed either an interstitial binding mechanism or a vacancy exchange mechanism [8]. Fig. 15 shows the grain boundary composition measurements in Fe–20Cr–24Ni, the predictions using an inverse Kirkendall description

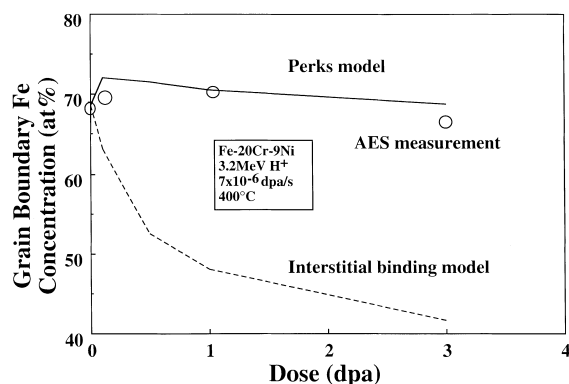


Fig. 14. Grain boundary Fe concentration in Fe–20Cr–9Ni irradiated at 400°C as a function of dose. Fe enriches at low (<1.0 dpa) dose and depletes at high doses (>3.0 dpa). The segregation measurements are compared to model calculations using (a) the Perks (inverse Kirkendall) model and (b) the interstitial binding model. Only the Perks model predicts the enrichment followed by depletion.

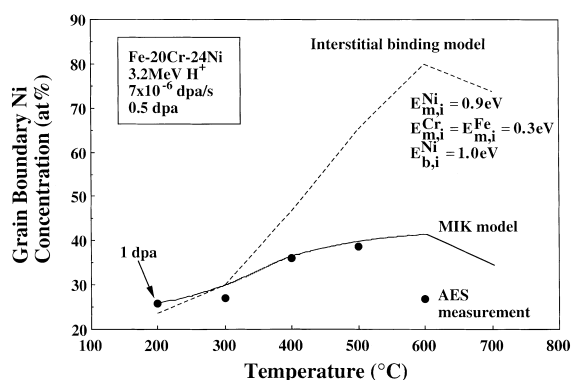


Fig. 15. Grain boundary Cr, Ni, and Fe concentration in Fe–20Cr–24Ni, measured by AES and plotted as a function of temperature. Measurements are compared to model calculations using the Perks model and to the interstitial binding model. For the interstitial binding model calculations, the interstitial migration and binding energies are listed.

of RIS where segregation is driven by the vacancy flux, and also by the interstitial binding model where binding of Ni to interstitials is included. The interstitial binding model severely overpredicts segregation, especially at temperatures between 400°C and 600°C. Ref. [3] outlines in detail, the failure of the interstitial binding model to predict the measured segregation, within the bounds of any reasonable model input parameters. Because the Perks model, which describes the RIS as primarily driven by the vacancy flux, slightly overpredicts the RIS measurements, any inclusion of interstitial binding will make the comparison between predicted and measured values worse. In fact, *any* choice of reasonable values of binding energy of Ni to interstitials (reasonable is defined as within the error band of experimental measurements) results in a temperature dependence that diverges from both the measurement and the prediction of the inverse Kirkendall model.

Additional evidence that the primary driving mechanism for RIS is the preferential interaction of solute atoms with the vacancy flux is provided in Fig. 16 in which the segregation behavior as a function of temperature is plotted for Ni–18Cr, Ni–18Cr–9Fe, and Fe–20Cr–24Ni. The minimum grain boundary Cr concentration occurs at the highest temperature in the Fe–20Cr–24Ni alloy and at the lowest temperature in the Ni–18Cr–9Fe alloy. From the RIS data, the migration energy would be expected to be largest in Fe–20Cr–24Ni and smallest in the Ni–18Cr–9Fe. The measured self-diffusion energies (E_{sd}^{Cr}) for Cr for each alloy are also compared in Fig. 16. As shown, the self-diffusion of Cr is largest in the alloys with the higher temperature of minimum grain boundary Cr concentration. For the alloys used in this segregation study, the smallest vacancy migration energy and thus the fastest segregation

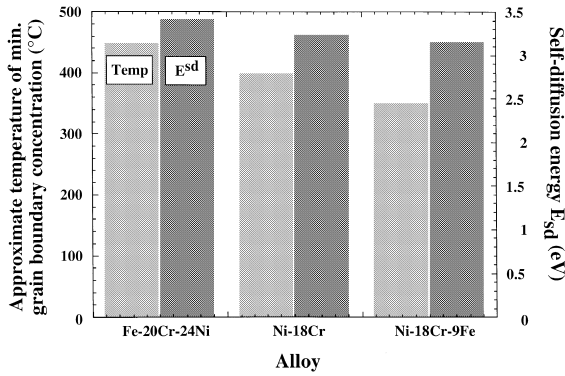


Fig. 16. Trends in temperature of minimum Cr concentration correspond with trends in self-diffusion energy. The concentration is consistent with the segregation being driven by preferential association of solutes with the vacancy flux.

is expected in the Ni–18Cr–9Fe alloy. Since the segregation behavior is consistent with trends predicted by self-diffusion energy (a function of interactions with vacancies), the temperature dependence of RIS is consistent with a vacancy effect.

The direction of segregation (enrichment or depletion) of Fe, Cr, and Ni in each of the alloys is also consistent with a vacancy mechanism. The equations describing RIS have been solved by Wiedersich et al. [49] to yield the relationship between an atom gradient and the vacancy gradient at steady-state for a binary alloy. The ratio of these two gradients has been termed the determinant (M) by Watanabe et al. [50]. For a binary alloy, the determinant for atom A is

$$M_A = \frac{\nabla C_A}{\nabla C_v} = \frac{C_A C_B d_{Ai} d_{Bi}}{\alpha (d_{Bi} C_B D_A + d_{Ai} C_A D_B)} \left(\frac{d_{Av}}{d_{Ai}} - \frac{d_{Bv}}{d_{Bi}} \right). \quad (11)$$

If the term

$$\left(\frac{d_{Av}}{d_{Ai}} - \frac{d_{Bv}}{d_{Bi}} \right)$$

is positive, the gradient of atom A is in the same direction as the vacancy gradient and atom A would deplete. Watanabe et al. [50] derived an expression for the determinant for atom j in a ternary alloy:

$$M_j = \frac{\nabla C_j}{\nabla C_v} = \frac{\frac{d_{jv} C_j}{D_j} \sum_{k \neq j} \frac{d_{kv} C_k}{D_k} - \frac{d_{jv} C_j}{D_j} \sum_{k \neq j} \frac{d_{kv} C_k}{D_k}}{\alpha \sum_k \frac{d_{kv} C_k}{D_k}}. \quad (12)$$

If the determinant for the j th atom is positive, then the j th atom depletes during irradiation.

Table 2 shows the Cr, Fe, and Ni determinants calculated for all seven alloys assuming that preferential coupling with the vacancy flux causes the segregation. The interstitial diffusivities were assumed equal for Cr, Fe, and Ni. The segregation trends (enrichment or depletion at the grain boundary) for Cr, Fe, and Ni that were seen in the RIS measurements are also listed. For each alloy where the determinant for the element is positive, depletion occurs; where the determinant is negative enrichment occurs. Note that for each element in each of the seven alloys studied, there is not one disagreement between measurement (by either STEM/EDS or AES) and calculation.

Two previously discussed issues also support a vacancy mechanism. In Fig. 12, the pre-exponential factors were shown to change with alloy composition. These pre-exponential factors change in a manner consistent with the change in self-diffusion coefficients [43], indicating that RIS is driven by a preferential interaction of solute atoms with the vacancy flux. Additionally, the segregation of Fe in Fe–20Cr–9Ni was shown to increase and then decrease as a function of dose. This behavior is predicted by a vacancy mechanism, but not by the interstitial binding mechanism. The interstitial binding model predicts that the Fe concentration will deplete rapidly as a function of dose, a behavior not seen in the composition measurements. *A detailed analysis of segregation in proton irradiated Fe–Cr–Ni alloys indicates*

Table 2

Segregation behavior in two nickel-base and five iron-base austenitic alloys compared to inverse Kirkendall predictions (determinants (M) calculated using Eq. (12))

Alloy	Direction of segregation from determinant			Refs.	Direction of segregation from measurement			Analysis method
	Cr	Fe	Ni		Cr	Fe	Ni	
Ni–18Cr	–	–	+	[51]	–/–	–	+/+	AES/STEM–EDS
Ni–18Cr–9Fe	–	–	+	[44]	–/–	–/–	+/+	AES/STEM–EDS
Fe–20Cr–9Ni	–	+	+	[43]	–/–	+/+	+/+	AES/STEM–EDS
Fe–16Cr–24Ni	–	–	+	[43]	–	–	+	AES
Fe–20Cr–24Ni	–	–	+	[43]	–/–	–/–	+/+	AES/STEM–EDS
Fe–24Cr–24Ni	–	–	+	[43]	–	–	+	AES
Fe–24Cr–19Ni	–	+	+	[43]	–	+	+	AES

+ Enrichment at grain boundary.

– Depletion at grain boundary.

that RIS in Fe–Cr–Ni alloys is driven primarily by an interaction of the solute atoms with the vacancy flux.

3.1.5. Segregation with proton irradiation compares favorably with neutron irradiation

The type of irradiating particle is not expected to affect RIS. Since RIS occurs by the preferential participation of alloying elements in defect fluxes *after* the primary knock-on interaction, RIS should be independent of irradiating species. This assumption can be tested by comparing grain boundary segregation as a function of alloy composition for both proton and neutron irradiation. Segregation measurements on a series of constant Cr, varying Ni alloys have been performed by Dumbill [52] (Fe–18Cr– x Ni–0.5Si–2.5Mo and Fe–18Cr– x Ni–0.5Si, where $x=15$ –30 at.%), Allen et al. [4] (Ni–18Cr–9Fe and Fe–20Cr–9Ni) and Damcott et al. [6] (Fe–20Cr– x Ni, where $x=9, 24$ at.%). The Ni–18Cr–9Fe and Fe–20Cr–9Ni alloys from Allen et al., along with the Fe–20Cr–24Ni alloy from Damcott, provide a series of alloys with constant Cr concentration near 20 at.% and Ni concentration varying from 9 to 72 at.%. The segregation for these constant Cr, varying Ni alloys (irradiated at temperatures from 400°C to 450°C) is plotted in Fig. 17 as the ratio of chromium depletion to nickel enrichment. This ratio decreases sharply with increasing nickel content in Fe-base alloys, regardless of irradiating particle. A similar trend was seen for constant Ni, varying Cr alloys [4] and is shown in Fig. 18. These results confirm the assertion that RIS in neutron- and proton-irradiated alloys follows the same type of behavior, independent of alloy composition. *Segregation behavior is similar for alloys irradiated with either neutrons or protons.*

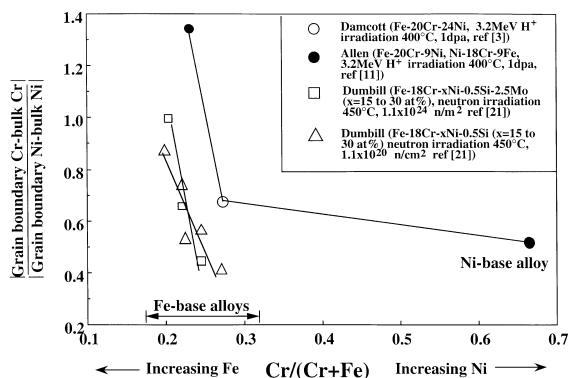


Fig. 17. Composition dependence of segregation for proton and neutron irradiated Fe–Cr–Ni alloys with constant Cr and varying Ni content.

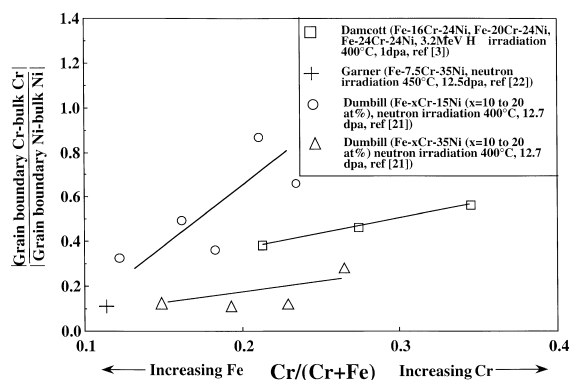


Fig. 18. Composition dependence of segregation for proton and neutron irradiated Fe–Cr–Ni alloys with constant Ni and varying Cr content [53].

3.2. Microstructure

A quantitative description of the irradiated microstructure is presented in Table 3 and Figs. 19–24 as a function of dose, temperature and alloy composition. Figs. 19 and 20 show that loop and void size and density increase for all alloys with increasing dose, but that the rate of increase with dose is alloy dependent. While the loop size and density in the Ni-base (Ni–18Cr–9Fe) alloy increases much quicker with dose than in the Fe-base alloys (Fe–20Cr–9Ni and Fe–20Cr–24Ni), the formation of voids is delayed. Figs. 21 and 22 show the temperature dependence of loop and void size and density for two Fe-base alloys. For both alloys, void and loop size increase sharply with irradiation temperature and the number density drops sharply. Figs. 23 and 24 provide alloy composition dependence of these microstructure features for fixed temperature/dose irradiation conditions. Note in Fig. 23 that both the loop size and density of the Ni-base alloy are considerably larger than those in Fe-base alloys, and are consistent with the suppression of voids in this alloy at the low dose and with neutron irradiation results [54]. Fig. 24 shows that minor elements can also affect the dislocation population. In fact, the behavior of the microstructure is closely linked to RIS. The following two sections show the link between RIS and dislocation microstructure and between RIS and void swelling.

3.2.1. Correlation between RIS and dislocation microstructure development

Both radiation-induced segregation and microstructural changes are dose-dependent, as shown in previous sections. However, both changes occur simultaneously during irradiation and are not independent of each other. In particular, as microstructure develops, the number of defect sinks in the alloy increases. With an increasing number of defect sinks, the flux of vacancies

Table 3
Measurements of dislocation and void microstructures in several austenitic alloys irradiated with 3.2 MeV protons

Alloy	Heat	T (°C)	Dose (dpa)	Disloc. loop diameter (nm)	Disloc. loop density (10^{15} cm^{-3})	Void diameter (nm)	Void density (10^{15} cm^{-3})	Refs.
Ni-18Cr-9Fe	RAM 1202	400	0.1	18	1.9	none	none	[16,21]
		400	0.3	13	2.6	none	none	[16,21]
		400	0.5	18	3.7	NM	0.07	[16]
		400	1.0	24	2.1	6.5	0.28	[16,21]
Fe-20Cr-24Ni	RAM 1155	400	0.5	16	1.3	7.8	1.7	[16,21]
		400	1.0	16	3.6	8.1	1.2	[16,21]
		400	3.0	16	4.7	8.2	2.4	[16,21]
		300	0.5	8.0	32	1.9	3.1	[21]
		500	0.5	49	0.092	12	0.10	[21]
		600	0.5	none	0	37	0.041	[21]
Fe-20Cr-9Ni	RAM 1327	400	0.1	13	0.5	< 4	0.02	[16]
		400	0.5	16	1.5	7.9	0.50	[16]
		400	3.0	23	2	14	0.93	[16]
		335	1.0	8.0	26	3.9	6.7	
		360	1.0	12	5.5	6	1.8	
Fe-20Cr-9Ni (UHP)	BPV 945	400	1.0	16	5.6	NM	NM	[10]
Fe-20Cr-9Ni-P (UHP + P)	BPV 603	400	1.0	27	5.7	NM	NM	[10]
Fe-20Cr-9Ni-S (UHP + S)	BPV 946	400	1.0	14	9.4	NM	NM	[10]
Fe-20Cr-9Ni-Si (UHP + Si)	BPV 604	400	1.0	10	10	NM	NM	[10]
Fe-18Cr-8Ni (commercial 304 SS)		360	1.0	8.2	17	none	none	
Fe-16Cr-13Ni (commercial 316 SS)		360	1.0	8.1	14	none	none	

NM: not measured.

to an individual sink (and corresponding flux of Cr away from a sink) is reduced. Thus, RIS may be affected by a developing microstructure.

Measurement of the dose dependence of both RIS and microstructure from the same alloy allows a direct comparison between the evolution of microchemical and microstructural changes. This comparison is made for Fe-20Cr-24Ni and Ni-18Cr-9Fe in Fig. 25. For the Fe-20Cr-24Ni alloy, both the grain boundary composition and the dislocation microstructure reach steady state by about 1 dpa. However, in the nickel-base alloy, steady state is achieved much sooner, between 0.1 and 0.3 dpa. The critical difference between these two alloys is that the self-diffusion energy is lower in the Ni-base alloy than in the Fe-base alloy, allowing for a much

more rapid development of segregation and dislocation microstructure. *Microstructure and microchemistry development under irradiation are linked and are dependent on the alloy diffusivity.*

3.2.2. Correlation between RIS and swelling

Microstructure characterization of Fe-Cr-Ni alloys irradiated with protons has also included a measurement of void size and density as a function of alloy composition. The void size and density were used to calculate the swelling in these alloys. Swelling as a function of composition in the proton-irradiated alloys was very similar to that in neutron- and ion-irradiated alloys. Fig. 26 shows void swelling as a function of bulk Ni composition for alloys irradiated with neutrons,

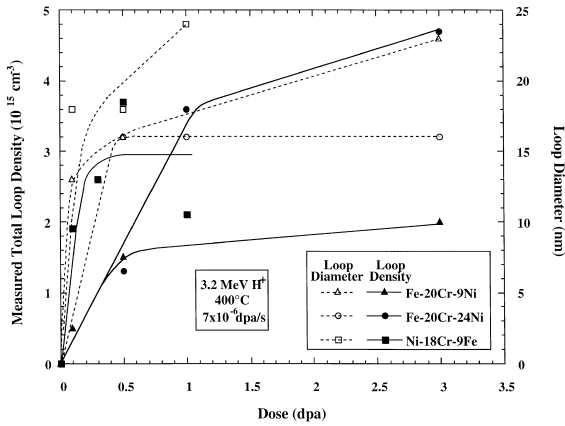


Fig. 19. Dose dependence of dislocation loop density and size for Fe-20Cr-9Ni, Fe-20Cr-24Ni and Ni-18Cr-9Fe at an irradiation temperature of 400°C.

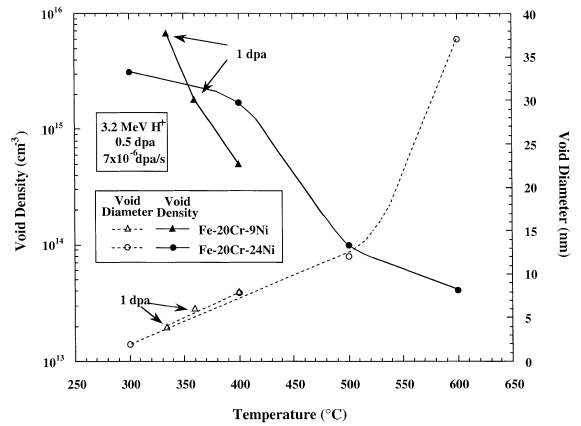


Fig. 22. Temperature dependence of void density and size for Fe-20Cr-9Ni and Fe-20Cr-24Ni at a dose of 0.5 dpa.

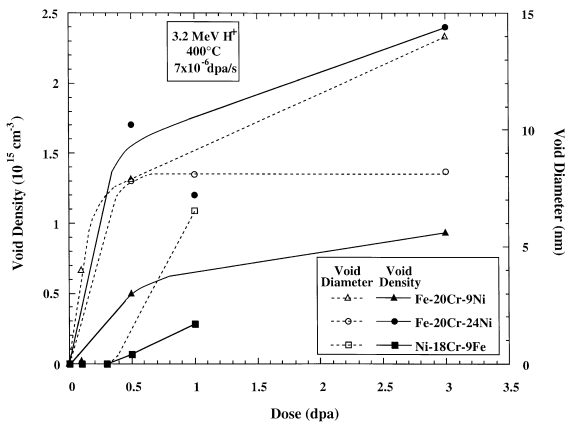


Fig. 20. Dose dependence of void density and size for Fe-20Cr-9Ni, Fe-20Cr-24Ni and Ni-18Cr-9Fe at an irradiation temperature of 400°C.

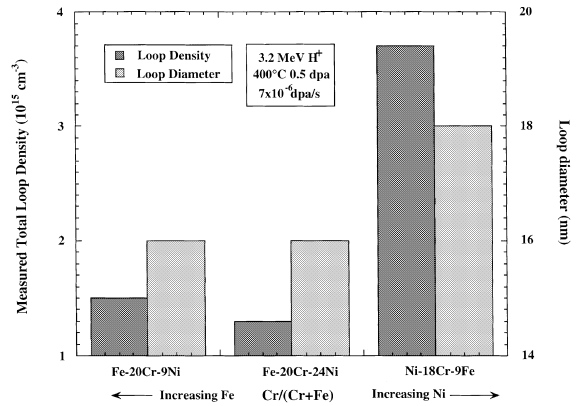


Fig. 23. Composition dependence of dislocation loop density and size for Fe-20Cr-9Ni, Fe-20Cr-24Ni and Ni-18Cr-9Fe at $T_{irr} = 400^\circ\text{C}$ and a dose of 0.5 dpa.

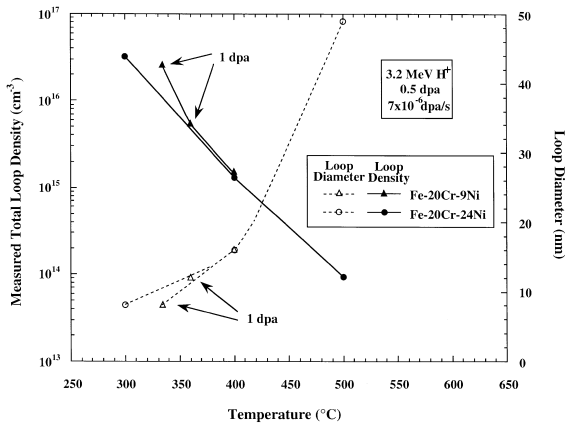


Fig. 21. Temperature dependence of dislocation loop density and size for Fe-20Cr-9Ni and Fe-20Cr-24Ni at a dose of 0.5 dpa.

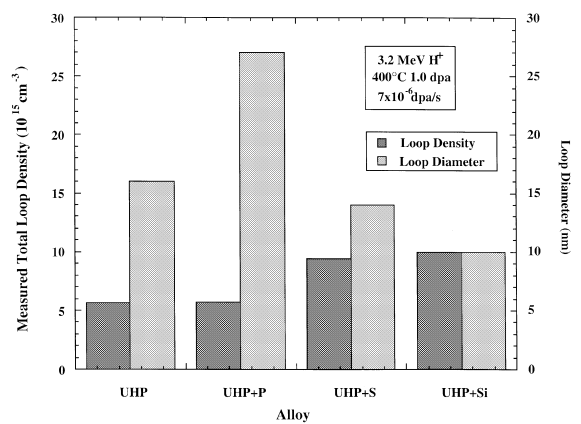


Fig. 24. Composition dependence of dislocation loop density and size for Fe-20Cr-9Ni, containing P, S and Si at $T_{irr} = 400^\circ\text{C}$ and a dose of 1.0 dpa.

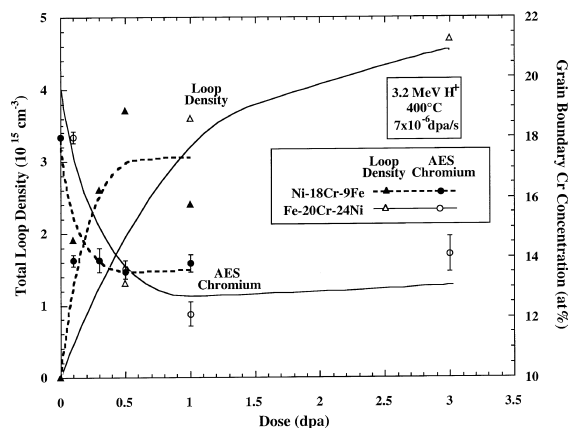


Fig. 25. Dose dependence of loop density and grain boundary Cr concentration (via AES) in Fe-20Cr-24Ni and Ni-18Cr-9Fe.

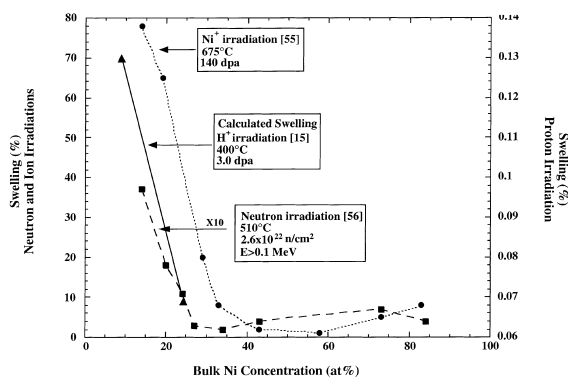


Fig. 26. Swelling as a function of bulk composition is similar for alloys irradiated with protons, neutrons and Ni^+ ions. Swelling measurements from the neutron irradiation has been multiplied by a factor of 10 to more clearly indicate the swelling trends [55,56].

protons, and Ni^+ ions. The swelling trends are the same regardless of irradiating particle.

The measurements of void size and density also showed that the rate of swelling was directly related to the composition changes at the void surface [15]. Enrichment of nickel and depletion of chromium reduced the vacancy flux to voids and thus limited the rate of void growth. Resistance to void swelling from major element segregation was calculated using the diffusivities inferred from segregation measurements and those alloys with the largest calculated resistance to swelling did indeed, swell the least. Therefore, a direct correlation was established and the composition dependence of diffusivities determined using RIS measurements was confirmed with independent swelling measurements. *Swelling and RIS display a similar composition depen-*

dence. Swelling is strongly influenced by the segregation of major elements at the void surface.

4. Summary

These results and the accompanying interpretations serve to underscore the utility of studying irradiation effects over a range of key parameters such as dose, temperature and alloy composition. Careful selection of parameters in concert with an understanding or hypothesis of the underlying mechanism were used to construct experiments which yielded a much better understanding of RIS and microstructure development under irradiation. We now know that:

- RIS of the major elements in Fe-Cr-Ni alloys is controlled by vacancy diffusion,
- the difference in migration energies between alloy constituents is critical in understanding RIS,
- the diffusivities of alloy constituents depend on the alloy composition and must be accounted for to accurately predict RIS,
- ordering is a significant factor influencing RIS in Ni-base austenitic alloys,
- the behavior of Fe at the grain boundary is a function of the alloy composition which dictates whether it enriches or depletes,
- void swelling and RIS show a similar composition dependence, providing independent confirmation of the dependence of diffusivity on alloy composition,
- RIS and dislocation microstructure development are governed by the same point defect kinetics and tend to develop at comparable rates in a given alloy, and
- the dependence of RIS in Fe-Cr-Ni alloys is consistent between proton and neutron irradiation.

Acknowledgements

The authors gratefully acknowledge S. Bruemmer, P. Andresen, L. Rehn, J. Cookson and L. Nelson for their many insightful comments and assistance. The authors also acknowledge the facilities provided by the Michigan Ion Beam Laboratory for Surface Modification and Analysis, and the Electron Microbeam Analysis Laboratory. This project was supported by the Department of Energy under grants DE-FG02-89ER-7552 and DE-FG02-93ER12130, and by Pacific Northwest National Laboratory. Research was sponsored by US Department of Energy, Division of Materials Sciences under contract DE-AC05-96OR22464 with Lockheed Martin Energy Research Corp., through the ShaRE User Program under contract DE-AC05-76OR00033 the Oak Ridge Associated Universities.

References

- [1] G.S. Was, P.L. Andresen, *JOM* 44 (4) (1992) 8.
- [2] T. Allen, G.S. Was, *Acta Metall.* 46 (10) (1998) 3679.
- [3] T. Allen, J.T. Busby, G.S. Was, E.A. Kenik, *J. Nucl. Mater.* 255 (1998) 44.
- [4] T. Allen, G.S. Was, E. Kenik, *J. Nucl. Mater.* 244 (1997) 278.
- [5] D. Damcott, J. Cookson, V. Rotberg, G.S. Was, *Nucl. Instrum. and Meth. B* 99 (1995) 780.
- [6] D. Damcott, T. Allen, G.S. Was, *J. Nucl. Mater.* 225 (1995) 97.
- [7] G.S. Was, S.M. Bruemmer, *J. Nucl. Mater.* 216 (1994) 348.
- [8] R.D. Carter, D.L. Damcott, M. Atzmon, G.S. Was, S.M. Bruemmer, E.A. Kenik, *J. Nucl. Mater.* 211 (1994) 70.
- [9] G.S. Was, T. Allen, *Mater. Char.* 32 (4) (1994) 239.
- [10] J. Cookson, R. Carter, D. Damcott, G.S. Was, M. Atzmon, *J. Nucl. Mater.* 202 (2) (1993) 104.
- [11] G.S. Was, T. Allen, *J. Nucl. Mater.* 205 (1993) 332.
- [12] D. Carter, D. Damcott, M. Atzmon, G.S. Was, E.A. Kenik, *J. Nucl. Mater.* 205 (1993) 361.
- [13] D.L. Damcott, J.R. Cookson, R.D. Carter, J.R. Martin, M. Atzmon, G.S. Was, *Rad. Eff. Def. Solids* 118 (1991) 383.
- [14] T.R. Allen, J.T. Busby, E.A. Kenik, G.S. Was, *Proceedings of Materials Research Society, Pittsburgh, Spring, 1998*, vol. 257, 1998, p. 291.
- [15] T.R. Allen, J.T. Busby, E.A. Kenik, G.S. Was, (submitted to Effects of Radiation on Materials) 19th International Symposium, American Society for Testing and Materials, Seattle, June, 1998.
- [16] J.T. Busby, T.R. Allen, J. Gan, G.S. Was, E.A. Kenik, *Proceedings of Eighth International Symposium on Environmental Degradation of Materials in Nuclear Power Systems – Water Reactors*, American Nuclear Society, LaGrange, IL, 1997, p. 758.
- [17] T.R. Allen, G.S. Was, in: R.K. Nanstad, M.L. Hamilton, F.A. Garner, A.S. Kumar (Eds.), *Effects of radiation on materials: 18th International Symposium*, ASTM STP 1325, American Society for Testing and Materials, 1997, in press.
- [18] J.T. Busby, T.R. Allen, E.A. Kenik, G.S. Was, *Proceedings of Materials Research Society, Pittsburgh*, vol. 439, 1997, p. 563.
- [19] T.R. Allen, G.S. Was, *Proceedings of Materials Research Society, Pittsburgh*, vol. 439, 1997, p. 539.
- [20] T.R. Allen, J.M. Cookson, D.L. Damcott, G.S. Was, *Proceedings of Materials Research Society, Pittsburgh*, vol. 439, 1997, p. 557.
- [21] J. Gan, T. Allen, G.S. Was, *Proceedings of Materials Research Society, Pittsburgh*, vol. 439, 1997, p. 445.
- [22] S.M. Bruemmer, J.I. Cole, R.D. Carter, G.S. Was, *Proceedings of Materials Research Society, Pittsburgh*, vol. 439, 1997, p. 437.
- [23] R. Dean Carter, M. Atzmon, G.S. Was, *Proceedings of Seventh International Symposium on Environmental Degradation of Materials in Nuclear Power Systems – Water Reactors*, NACE International, Houston, TX, 1995, p. 807.
- [24] T.R. Allen, D.L. Damcott, G.S. Was, *Proceedings of Seventh International Symposium on Environmental Degradation of Materials in Nuclear Power Systems – Water Reactors*, NACE International, Houston, TX, 1995, p. 997.
- [25] J.M. Cookson, G.S. Was, P.L. Andresen, *Proceedings of Seventh International Symposium on Environmental Degradation of Materials in Nuclear Power Systems – Water Reactors*, NACE International, Houston, TX, 1995, p. 139.
- [26] T.R. Allen, G.S. Was, *Proceedings of Materials Research Society, Pittsburgh*, vol. 373, 1995, p. 101.
- [27] R.D. Carter, M. Atzmon, G.S. Was, S.M. Bruemmer, *Proceedings of Materials Research Society, Pittsburgh*, vol. 373, 1995, p. 171.
- [28] D.L. Damcott, G.S. Was, S.M. Bruemmer, *Proceedings of Materials Research Society, Pittsburgh*, vol. 373, 1995, p. 131.
- [29] E.A. Kenik, R.D. Carter, D.L. Damcott, M. Atzmon, G.S. Was, in: G.W. Bailey, A.J. Garrett-Reed (Eds.), *Proceedings of 52nd Annual Meeting of the Microscopy Society of America*, San Francisco Press, 1994, p. 96; also in: J. Friel (Ed.), *Microbeam Analysis, Proceedings of the 28th Annual Mass Meeting*, VCH, New York, 1994, p. 319.
- [30] S. Bruemmer, J. Cole, R. Carter, in: R.E. Gold, E.P. Simonen (Eds.), *Proceedings of the Sixth International Symposium on Environmental Degradation of Materials in Nuclear Power Systems – Water Reactors*, Minerals, Metals and Materials Society, Warrendale, PA, 1993, p. 537.
- [31] G.S. Was, R. Carter, D. Damcott, M. Atzmon, S. Bruemmer, E. Kenik, in: R.E. Gold, E.P. Simonen (Eds.), *Proceedings of the Sixth International Symposium on Environmental Degradation of Materials in Nuclear Power Systems – Water Reactors*, Minerals, Metals and Materials Society, Warrendale, PA, 1993, p. 501.
- [32] J. Cookson, R. Carter, G.S. Was, P. Andresen, in: R.E. Gold, E.P. Simonen (Eds.), *Proceedings of the Sixth International Symposium on Environmental Degradation of Materials in Nuclear Power Systems – Water Reactors*, Minerals, Metals and Materials Society, Warrendale, PA, 1993, p. 573.
- [33] G.S. Was, M. Atzmon, J. Cookson, D. Damcott, D. Carter, in: P.K. Liaw, R. Viswanathan, K.L. Murty, E.P. Simonen, D. Frear (Eds.), *Proceedings, Microstructures and Mechanical Properties of Aging Materials*, The Minerals, Metals and Materials Society, Warrendale, PA, 1993, p. 349.
- [34] R.D. Carter, J.R. Cookson, D.L. Damcott, M. Atzmon, G.S. Was, *Proceedings of the Fifth International Symposium on Environmental Degradation of Material in Nuclear Power Systems – Water Reactors*, American Nuclear Society, 1992, p. 806.
- [35] TRIM97 Program, J.F. Ziegler, J.P. Biersack, IBM Corp. Yorktown, NY, 1997.
- [36] T.R. Allen, PhD thesis, University of Michigan, 1997.
- [37] L.E. Davis, N.C. MacDonald, P.W. Palmberg, G.E. Riach, R.E. Weber, *Handbook of Auger Electron Spectroscopy*, 2nd ed., Perkin Elmer, Eden Prairie, MN.
- [38] E.A. Kenik, *Scripta Metall.* 21 (1987) 811.
- [39] T. Sawai, M. Suzuki, DOE/ER-0313/6, US Department of Energy, Oak Ridge National Laboratory, March 1989.

- [40] J.F. Mansfield, D.C. Crawford, in: L.D. Peachy, D.B. Williams (Eds.), *Proceedings of the 12th International Congress on Electron Microscopy*, Seattle, WA, vol. 2, Analytical Sciences, San Francisco Press, San Francisco, 1990, p. 504.
- [41] M.L. Jenkins, *J. Nucl. Mater.* 216 (1994) 124.
- [42] J.M. Perks, A.D. Marwick, C.A. English, Harwell Laboratory, Oxfordshire, UK, AERE R 12121, June 1986.
- [43] S.J. Rothman, L.J. Nowicki, G.E. Murch, *J. Phys. F* 10 (1980) 383.
- [44] B. Million, J. Ruzickova, J. Vrestal, *Mater. Sci. Eng.* 72 (1985) 85.
- [45] P. Cenedese, F. Bley, S. Lefebvre, *Acta Crystall. A* 40 (1984) 228.
- [46] A.D. Marwick, R.C. Piller, T.E. Cranshaw, *J. Phys. F* 17 (1987) 37.
- [47] A. Marucco, *Mater. Sci. Eng. A* 189 (1994) 267.
- [48] C. Dimitrov, D. Huguenin, P. Moser, O. Dimitrov, *J. Nucl. Mater.* 174 (1990) 22.
- [49] H. Wiedersich, P.R. Okamoto, N.Q. Lam, *J. Nucl. Mater.* 83 (1979) 98.
- [50] S. Watanabe, H. Takahashi, *J. Nucl. Mater.* 208 (1994) 191.
- [51] J. Ruzickova, B. Million, *Mater. Sci. Eng.* 50 (1981) 59.
- [52] S. Dumbill, PhD thesis, University of Birmingham, 1992.
- [53] F.A. Garner, A.S. Kumar, in: F.A. Garner, N.H. Packan, A.S. Kumar (Eds.), *ASTM STP 955*, American Society for Testing and Materials, Philadelphia, 1987, p. 289.
- [54] R.K. Bullough, J.K. Jenkins, T.M. Williams, *Proceedings of the International Conference on Materials for Nuclear Core Applications*, vol. 1, British Nuclear Energy Systems, London, 1987, p. 285.
- [55] W.G. Johnston, J.H. Rosolowski, A.M. Turkalo, T. Lauritzen, *J. Nucl. Mater.* 54 (1974) 24.
- [56] J.F. Bates, W.G. Johnston, *Proceedings of the International Conference on Radiation Effects in Breeder Reactor Structural Materials*, Scottsdale, New York, The Metallurgical Society of AIME, Warrendale, PA, 1977, pp. 625–644.